Morphology and Mechanical Properties of Copolymer Ethylene−Methyl Methacrylate Films as a Function of Temperature Estimated by Polarized Light Scattering, X-ray, and ^{13}C NMR

Lin Ma, Yuezhen Bin, Yuko Sakai, Qun Chen,† Hiromichi Kurosu, and Masaru Matsuo*

Department of Textile and Apparel Science, Faculty of Human Life and Environment Nara Women's University, Nara 630-8263, Japan

Received December 12, 2000; Revised Manuscript Received April 9, 2001

ABSTRACT: The relationship between the morphology and the mechanical properties of copolymer ethylene−methyl methacrylate (EMMA) was estimated as a function of temperature by using polarized light scattering, X-ray diffraction and ^{13}C solid-state NMR. All of these measurements revealed unstable crystallites within the EMMA films having a MMA content >14 mol %, crystallinity less than 10%, and crystal size of about 3 nm. On the other hand, the ethylene sequences in the amorphous phase had an ordered arrangement rather than a random orientation. It is evident that these characteristics are due to the strong repulsion between MMA and ethylene. Namely, MMA side groups suppress the crystallization as an essential property of ethylene sequences; consequently, the difficulty of accelerating the self-arrangement of ethylene sequences as crystallites leads to a local ordered arrangement of long ethylene sequences in the amorphous phase. The maximum draw ratio of the EMMA film reached 10 times at room temperature. A specimen with a draw ratio <2 showed a reversible change of stress−strain curves up to 40 repetitions at room temperature. This behavior appears to be within the framework of ideal rubber elasticity. However, the stress at a fixed strain decreased with passing time as well as with increasing temperature. This behavior is completely out of the framework. Such inconsistency is due to the fact that small crystallites playing a cross-linking role became disrupted by chain slippage at a constant strain and at elevated temperature.

1. Introduction

There has been considerable interest in the past three decades in clarifying the intrinsic properties of the amorphous phase of polymeric systems. As a general concept of the amorphous phase of noncrystalline polymers, Flory proposed a random coil model with a number of entanglements and pointed out that the size of the coil is equal to the expansion calculated by a nonperturbation method.[1] On the basis of electron microscopy, Yeh proposed a model in which the amorphous phase consists of ordered and disordered regions,[2] while Pechold et al. proposed a meander model based on thermodynamics.[3] Vollmert and Stutz pointed out that the amorphous phase is made up of isolated crashed-like coils.[4] Recent developments in X-ray and neutron scattering have provided a new method to separate the scattering information associated with a chain from that associated with a polymer chain matrix by using polymer tagged by heavy hydrogen.[5−6] The results supported the concept of Flory[1] that the amorphous phase consists of random coils with almost the same inertia radius as in a Θ solvent. Even so, this conclusion still leaves unresolved problems in application to the amorphous phase of semicrystalline polymers. Although solid polyethylene (PE) is a typical example of a semicrystalline polymer, its amorphous structure is unknown because of the difficulty of preparing specimens with very low crystallinity, which is due to the considerable crystallization associated with the essential properties of ethylene sequences.

To obtain a large amount of amorphous ethylene sequences, a series of ethylene copolymers, ethylene−dimethylaminoethyl methacrylate (EDAM),[7−9] and cycloolefin copolymers (COCs)[10] are useful specimens. For EDAM, the CH_2 groups neighboring dimethylaminoethyl (DAM) units are excluded from the crystalline regions, but the ethylene chains between two DAM groups can form crystallites that provide X-ray diffraction peaks similar to branched PE. Incidentally, the X-ray diffraction profile and DD ^{13}C NMR spectrum of branched PE are essentially the same as those of linear PE. The detailed analyses by Vander Hart et al. and Perez et al.[11−12] demonstrated that some methyl and ethyl short branches and cross-linking carbons enter the crystalline regions as defects, although their concentration is much lower than that in the amorphous (noncrystalline) region. On the other hand, COCs provide X-ray intensity distribution with a broad peak at 17° (twice the Bragg angle), indicating scattering from the amorphous phase and no existence of an orthorhombic crystal form.[12] This means that the crystallization of ethylene main chains is strongly interrupted by the steric hindrance of side groups and norbornene units. To study the effect of side groups on the crystallization of ethylene main chains, this paper deals with Ethylene-Methyl methacrylate (EMMA), which is a copolymer of

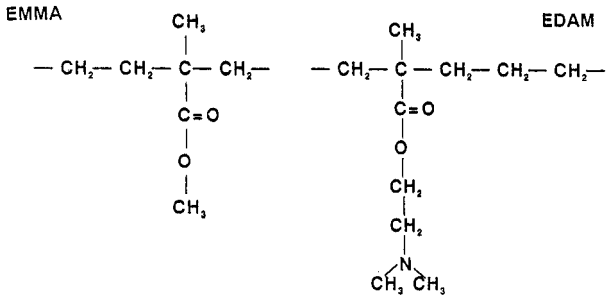

ethylene and methyl methacrylate (MMA) manufac-

* To whom all correspondence should be addressed.

† On leave from East China Normal University, Shanghai, China by the financial support of Japan Society for Promotion of Science.

10.1021/ma002110w CCC: $20.00
Published on Web 06/06/2001

Table 1. Characterization of EMMA and EDAM

specimen	mol %	mp (°C)	draw ratio (max.)	mol wt $\bar{M}_n$ ($\times 10^4$)	mol wt $\bar{M}_w$ ($\times 10^4$)
EMMA-I (WD201)	3.0	100	5	4.7	
EMMA-II (WH202)	6.5	85	6	4.3	
EMMA-III (WM403)	14.6	64	10	3.1	
EDAM-I (DA3023)	3.9	97	1.6	2.43	8.88
EDAM-II (DA3031)	4.1	66	1.6	2.93	8.29
LDPE (G201)	5.3[b]	104	4.6	4.13[a]	

[a] $\bar{M}_v$ ($\times 10^4$). [b] 2.8CH_3/100 °C.

tured by a high-pressure radical polymerization process common to low-density polyethylene (LDPE).[8] According to detailed studies at the industrial level, it has been reported that the rigidity, yield stress, impact strength, and gas permeability depend on the content of MMA as side groups. In a preliminary experiment, the thermal decomposition of EMMA starts at 330 °C. This temperature is similar to that of LDPE and higher than that of ethylene−vinyl alcohol copolymer (EVOH). This indicates that the thermal stability of EMMA is better than that of EVOH.

Despite the many studies on branched PE, EDAM, and EVOH, few papers have examined the detailed morphology and mechanical properties of EMMA films with different MMA contents.[13] Accordingly, the characteristics of EMMA films are investigated in comparison with the characteristics of EDAM and branched PE in order to elucidate the important relationship between morphology and molecular dynamics.

2. Experimental Section

EMMA, EDAM random copolymer and PE samples were furnished from Sumitomo Chemical Co. Ltd., and the chemical structures and the characteristics are listed in Table 1. The EMMA specimens with different contents of side groups of MMA were termed as EMMA-I, EMMA-II and EMMA-III. A similar classification was done for the EDAM specimens. The signs in bracket such as WD201 and DA3023 are commercial names. The pellets of EMMA and EDAM were pressed at 150 °C under 0.5 MPa and the molded specimen was cooled to room temperature. The thickness of all the specimens were about 300 μm.

The melting point was estimated by differential scanning calorimetry (DSC). The specimens, weighing 5 mg, were placed in a standard aluminum sample pan. Samples were heated at a constant rate of 1 °C/min. With increasing content of MMA side groups beyond 6.5 mol % and DAM side groups beyond 4.1 mol %, the melting point became lower, indicating very small crystallinity and very small crystal size. Comparing the maximum draw ratios of EMMA-I and EMMA-II films with those of EDAM-I and EDAM-II films, it is evident that chemical structure of side group influences the maximum draw ratio. These results indicate that the melting point and maximum draw ratio are hardly affected by molecular weight but are sensitive to the content of side groups. Incidentally, the same characteristics listed in Table 1 were measured for annealed specimens but all the data for the EMMA and EDAM films were almost the same as those for the quenched films, independent of heat-treatment. Such a no-heat-treatment effect has been observed for many kinds of PE films.

Small angle light scattering (SALS) patterns were obtained with a 3 mW He−Ne gas laser as a light source. Diffuse scattering was avoided by sandwiching the specimen between cover glasses with silicon oil as an immersion fluid.

The X-ray measurements were carried out with a 12 kW rotating-anode X-ray generator (Rigaku RAD-rA). WAXD patterns were obtained with a flat camera using CuK_α radiation at 200 mA and 40 kV. The X-ray beam was monochromatized with a curved graphite monochromator. SAXS intensity was detected with a position-sensitive proportional counter (PSPC). Time resolution of WAXD was carried out by using a curved PSPC to estimate the change in diffraction intensity distribution as a function of twice of the Bragg angle under the stress relaxation process. To pursue the accuracy of accumulation of the intensity, the measured period was set to be 200 s.

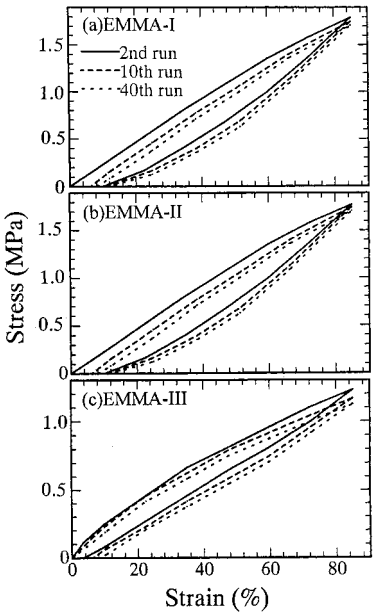

Figure 1. Stress−strain curves for three kinds of EMMA films, EMMA-I, EMMA-II, and EMMA-III repeated up to 40 times measured at 25 °C.

To measure stress−strain recovery, elongation was done at 30 °C with an Instron tester at the cross head speed of 1.8 mm/min. The initial dimensions of the samples were as follows: length 100 mm and width 20 mm.

NMR measurements were carried out for the EMMA melt films as a function of temperature by a JEOL, JM-EX270 spectrometer, operating at 67.8 MHz for ^{13}C. Room temperature and 60 °C were adopted for the measurements. The actual temperatures in the probe under spinning were confirmed to be in the ranges 27−36 and 60−64 °C respectively. The magic-angle spinning rate was 5−5.5 kHz. The contact time in ^{13}C CP/MAS measurement was 2 ms. The chemical shifts were determined relative to the higher field signal (29.5 ppm) of adamantine. ^{13}C spin−lattice relaxation times (T_{1C}) longer than several tens of seconds were estimated on the basis of the method developed by Torchia, while T_{1C} shorter than a few seconds was measured by employing the standard saturation-recovery pulse sequence without CP.

3. Results and Discussion

3.1. Stress−Strain Behavior. Figure 1 shows repeated curves of stress−strain, in which films were stretched up to $\lambda = 1.85$ and then recovered. Parts a−c show the behavior of three kinds of undrawn EMMA films: EMMA-I, EMMA-II, and EMMA-III. Interestingly, the repeated curves for the specimens pass through almost the same route up to the 40th run. Such reversible behavior is similar to rubber elasticity, although hysteresis between the stretching and recovering routes is observed. Such good reversible behavior has never been observed for any kind of polyethylene film or fiber, even when the drawn ratio is less than 1.1.

When the draw ratio increases beyond $\lambda = 3$, the stress increases and the curve deviates from the recycle routes, indicating a large deviation from rubber elasticity. This tendency was remarkable with decreasing

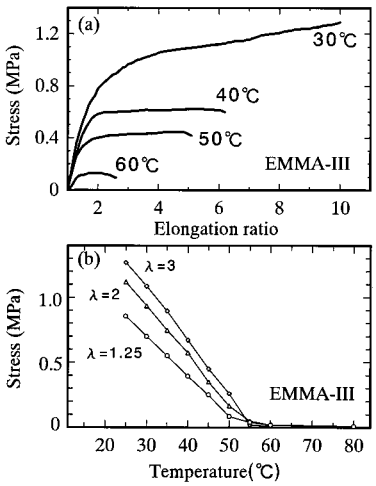

Figure 2. (a) Stress−strain curves of EMMA-III at the indicated temperatures, (b) Stress relaxation behavior of drawn EMMA-III film at elevated temperature.

MMA content. Incidentally, such reversible behavior was not observed for two kinds of EDAM films, EDAM-I and EDAM-II, even with a lower draw ratio than 1.1.

Figure 2a shows the stress−strain curve for the EMMA-III film. With increasing temperature, the maximum draw ratio and the stress at each draw ratio become less pronounced. No such drastic decrease in maximum draw ratio with temperature has ever been reported for PE and atactic polystyrene films. However, the decrease in stress at each draw ratio seems reasonable for ensuring significant drawability due to the smooth transmission of inner strain within linear thermoplastic polymers. The unusual tendency of the decreasing maximum draw ratio is also confirmed for other specimens, EMMA-I and EMMA-II, but it is less pronounced with increasing MMA content. The drastic decrease in stress seems to reflect the drastic slippage of molecular chains due to the disappearance of crystallites as cross-linking points at elevated temperatures followed by the inability of the inner stress within the specimen to transmit smoothly under elongation. This indicates that an increase in MMA side group hampers the growth of large crystallites and that the small crystallites become unstable at elevated temperatures. The justification of this analysis will be discussed later together with X-ray data. Figure 2b shows the temperature dependence of the stress measured for the EMMA-III film which were stretched up to $\lambda = 1.25$, 2, and 3 and maintained at the same draw ratio. The rate of temperature rise was 1 °C/min, and the measurement was done after maintaining the sample for 10 min at the fixed temperature. With increasing temperature, the stress decreases drastically. In addition to the unusual stress−strain curves in Figure 2a, the behavior shown in Figure 2b is also quite different from rubber elasticity. If the specimen follows rubber elasticity, as pointed by Merret,[13] the stress must increase with temperature.

3.2. Analysis by Polarized Light Scattering and X-ray. To study the main cause of the stress relaxation and great drawability (10 times) of EMMA-III, the influence of MMA side groups on mechanical properties was analyzed in terms of morphological aspects by using WAXD and SALS. The SALS patterns under Hv polarization showed no scattering in three kinds of undrawn EMMA films: EMMA-I, EMMA-II, and EMMA-III, indicating the absence of superstructures such as rods or spherulites. However very indistinct structures were observed under polarizing microscopy, and the corresponding WAXD patterns showed a diffraction ring. The magnitude of the ring became drastically weaker with increasing MMA content, indicating a drastic decrease in crystallinity. However, it should be noted that the elongation causes a significant effect on the development of superstructures within EMMA films as shown in Figure 3.

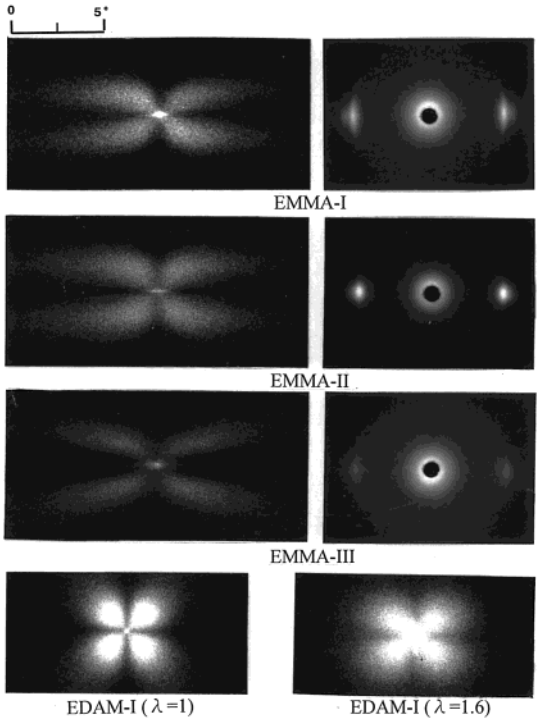

Figure 3. Hv patterns and the corresponding WAXD patterns for three kinds of EMMA films, EMMA-I, EMMA-II, and EMMA-III with $\lambda = 5$ and EDAM (EDAM-I) films at $\lambda = 1$ and 1.6.

When the EMMA samples were stretched up to 5 times and kept at the same draw ratio, an X-type pattern was observed under Hv polarization. The corresponding WAXD pattern showed diffraction spots in the equatorial direction. Incidentally, the SALS patterns from EDAM-I films with 3.9 mol % DAM side groups are shown together in this figure to emphasize that the appearance of superstructures depends on the characteristics of the side groups. It can be seen that the Hv scattering from the three kinds of EMMA films provides essentially the same X-type patterns with lobes extended in the horizontal direction, although the intensity magnitude decreases with increasing MMA content. The large difference in intensity is obviously due to the crystallinity. The scattered intensity at a given azimuthal angle continuously decreases with increasing scattering angle. In this regard, the patterns are typical of an oriented assembly of anisotropic rods.[14]

The X-ray diffraction spots become weaker with an increase in the MMA content and in particular, the spots from EMMA-III (14.6% MMA) become drastically weaker. This reflects the restrained crystallization of ethylene sequences due to the increase in MMA content. Here we must emphasize that Hv scattering from EMMA films with a draw ratio of <3 showed no X-type pattern, indicating that small crystallites dispersed in the amorphous regions without forming rods. On the basis of the stress−strain curves in Figure 1, we can draw the

interesting conclusion that the small crystallites play an important role as cross-linking points, and the strain is recovered and near zero with decreasing applied stress. This ensures smooth transmission of inner stress under the cyclic processes of elongation and shrinkage.

On the other hand, the pattern from EDAM-I film at $\lambda = 1$ (see bottom) shows a four-leaf clover type, indicating scattering from perfect spherulites with its maximum intensity at odd multiples of the azimuthal angle (μ) of 45°,[15] as has been observed for polyethylene (G201).[16] As shown in the pattern, the scattered intensity becomes zero at the scattering center ($\theta = 0°$), since the amplitude of scattering from different parts of the spherulite tends to cancel out at very small angles due to the symmetry of optical axis orientation and the distribution of scattering elements. The same patterns were also observed for EDAM-II films. The average radii of spherulites of EDAM-I and EDAM-II were 4.68 and 2.94 μm, respectively. The lobes were extended in the horizontal direction at $\lambda = 1.6$, and scattered intensity was not zero at $\theta = 0°$. This deviates from deformation of perfect spherulites associated with the change from a sphere to an ellipsoid while keeping uniform optical density within the spherulite. The nonuniform deformation causes large orientation fluctuations of the optical axes with respect to the radial direction and/or large optical density fluctuation within the spherulites.[16,17] Incidentally, X-ray diffraction patterns could not be observed, since the specimen kept at $\lambda = 1.6$ was cut after 1 h.

Judging from the different pattern profiles between EMMA (EMMA-I) and EDAM (EDAM-I and EDAM-II) with similar side group contents (see Table 1), the formation of superstructures is sensitive to the molecular structure of side groups. The DAM side group is bulkier than the MMA side group. The presence of different types of superstructures indicates that the MMA and DAM side groups have large but different influences on drawability. The ethylene sequence of EDAM-I (or EDAM-II) can form chain-folded lamellae that are a more or less regular aggregation of crystallites within spherulites. In this case, the amorphous chain segments forming folded loops have a very small possibility of forming tie molecules and/or entanglements to connect with the lamellae because of the strong repulsion between ethylene sequences and bulky DAM side groups. This concept helps to explain how the maximum draw ratios of EDAM films are less than 2 times those listed in Table 1. To pursue this concept, the stress relaxation with time and the change in Hv patterns are obtained for the EMMA and EDAM specimens.

When an EMMA-III specimen is stretched up to 10 times, the scattering shows the superposition of broad four-leaf lobes and sharp streaking as shown in Figure 4. The intensity of the streaks is much stronger than that of the lobes. Accordingly, the appearance of streaking is not due to the interparticle interference effects of rods, indicating that the gravity of each rod within an assembly is situated with respect to the stretching direction.[18−20] The streak is surely attributed to the fissures parallel to the stretching direction,[21] which were observed under polarized light microscopy. Here we must emphasize that silicon oil with a refractive index similar to the refractive index of the specimen was spread on the surface of the specimen at a fixed state. Actually, as shown in Figure 4, the streak was not

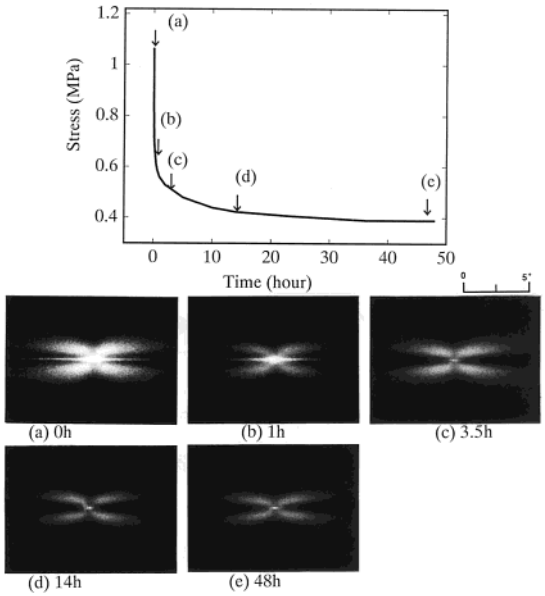

Figure 4. Stress−relaxation curve of the EMMA (EMMA-III) film with $\lambda = 10$ and the Hv patterns observed at the indicated times.

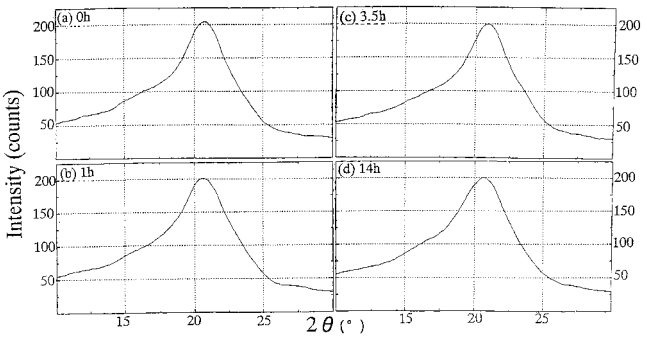

Figure 5. WAXD intensity distributions observed at the indicated times under stress relaxation process shown in Figure 4.

observed for the specimens after 3 h but observed within 1 h, because of insufficient immersion of the silicon oil into the fissures within the specimen. The X-type pattern is attributed to the presence of rods with high optical anisotropy taking a highly preferential orientation of the optical axes with respect to the rod axis.[13] When the specimen was maintained at the same draw ratio, the intensity became weaker and the streaks disappeared, reflecting the disruption of an assembly formed with an ordered orientation of rods with respect to the stretching direction. The corresponding time dependence of the applied stress indicates that drastic stress relaxation occurs within 1 h and the applied stress tends to level off. One month later, the scattered intensity became very weak but the profile of the X-type pattern was maintained. This suggests that the degree of the optical anisotropy of rods becomes smaller with time but the orientation of rods is independent of time. Under drastic stress−relaxation, the orientation of crystallites and the crystallinity were nearly maintained, and such behavior was confirmed by time-resolved X-ray diffraction intensity as shown in Figure 5. The X-ray diffraction intensity distribution in the horizontal direction was measured by setting the drawn direction along the vertical direction. It can be seen that the intensity distribution maintains an almost constant profile. Of course, the drastic stress relaxation is due

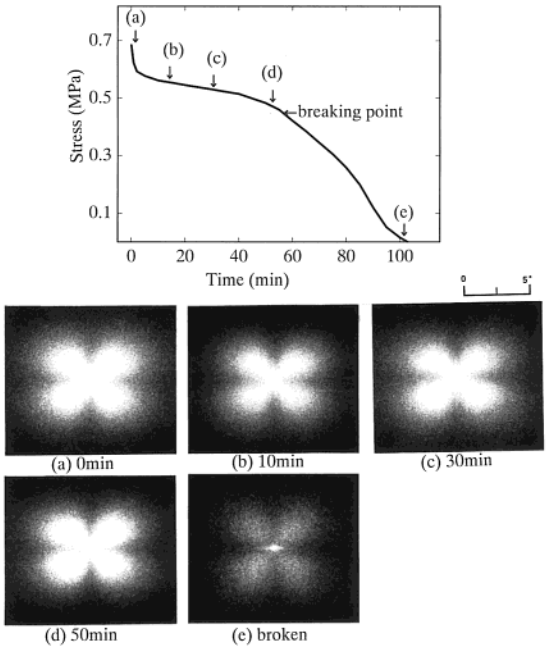

Figure 6. Stress−relaxation curve of EDAM (EDAM-II) and the Hv patterns observed at the indicated times.

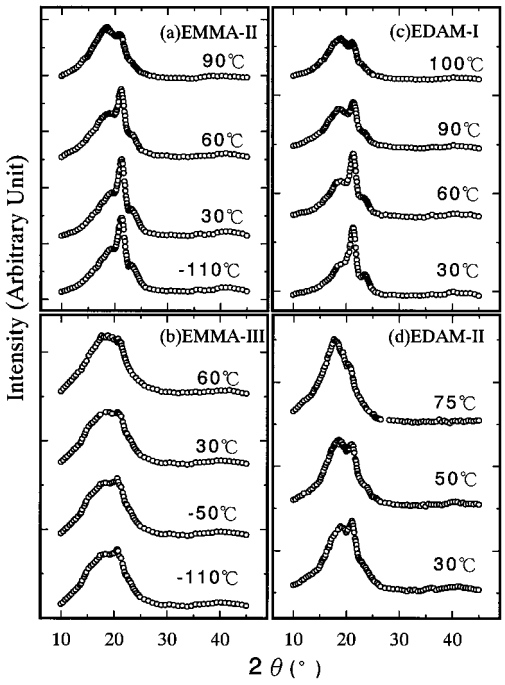

Figure 7. WAXD intensity distributions of undrawn EMMA (EMMA-II, EMMA-III) films and undrawn EDAM (EDAM-I, EDAM-II) films at elevated temperatures.

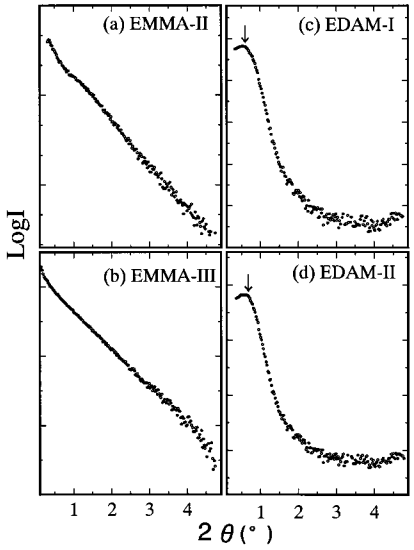

Figure 8. SAXS intensity distributions for EMMA (EMMA-II and EMMA-III) films and EDAM (EDAM-I and EDAM-II) films.

to molecular slippage by disentanglements. This causes less promotion of the scattered intensity by the disruption of the oriented rods.

In comparison with the EMMA-III films, Hv patterns from drawn EDAM-II films are shown in Figure 6. The pattern from the disordered spherulites shows no time dependence of scattered intensity and maintains the same profile before partial breaking of the specimen. The specimen was cut off after 110 min by the inner stress, which occurred at a constant external strain. This indicates that the DAM side groups strongly hamper the possibility of forming a sufficient number of tie molecules and/or chain entanglements between lamellae within the deformed spherulites and the shear slippage between the isolated lamellae causes destruction of the specimen. Here, it is important to ascertain whether crystallites within EMMA and EDAM films become unstable and induce the disruption of crystal lattice with increasing temperature. Therefore, WAXD intensity distributions were observed for the undrawn EMMA and EDAM films as a function of temperature. Corrections of X-ray diffraction intensity were made for air scattering, polarization, and absorption. The intensity curve thus obtained was assumed to be due to the contribution from the crystalline and amorphous phases.

Figure 7 shows the X-ray results for the undrawn EMMA (EMMA-II and EMMA-III) and EDAM (EDAM-I and EDAM-II) films, in which parts a and b of Figure 7 are the diffraction profiles for EMMA-II and EMMA-III, respectively. The specimens were maintained for 10 min at the indicated temperatures prior to the measurements. At 30 °C, the intensity distribution for EMMA-II is similar to the distribution of PE with low crystallinity. Namely, two peaks appeared at 21.5° and 23.3° (twice the Bragg angle), corresponding to the reflections from the (110) and (200) planes of polyethylene crystals, respectively. The large peak at 18.2° is attributed to the contribution from the amorphous phase. On the other hand, intensity distribution for the EMMA-III film shows two peaks at 21.5 and 18.2°, respectively, and no peak corresponding to the (200) reflection is observed, indicating very low crystallinity. This indicates that the crystallization of ethylene sequences is suppressed by an increase in MMA content. Parts c and d of Figure 7 show the intensity distributions of EDAM-I and EDAM-II films, respectively. For EDAM-I, the intensity distribution at 30 °C has three peaks similar to the profile of EMMA-II, but the distribution of EDAM-II with higher content of DAM is slightly similar to that of EMMA-III.

Despite the small differences in WAXD intensity distribution between EMMA (EMMA-III) and EDAM (EDAM-II) films, SAXS intensity distributions from both films showed different profiles (Figure 8) when an incident X-ray beam entered parallel to the film surface.

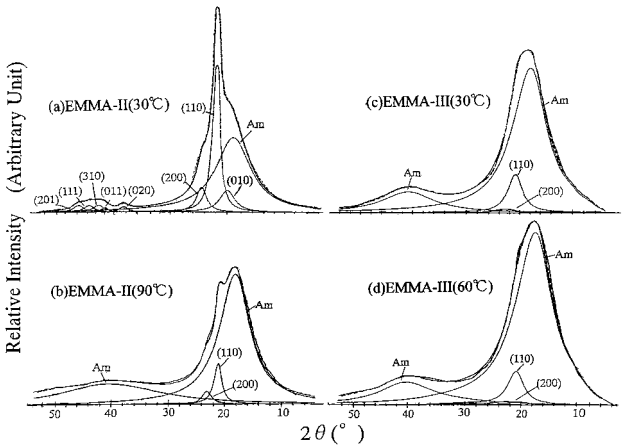

Figure 9. Component analysis of total WAXD intensity distributions for EMMA at the indicated temperature: (a) EMMA-II at 30 °C; (b)EMMA-II at 90 °C; (c) EMMA-III at 30 °C; (d) EMMA-III at 60 °C.

Detailed observation reveals that EMMA films give a monotonic curve while EDAM films give a curve with a scattering peak corresponding to a long period of about 8.8 nm. The existence of the long period was already reported for EDAM specimens.[8] The small peak implies the presence of crystal lamellae within two-dimensional EDAM spherulites, while no peak denotes the absence of crystal lamellae within EMMA films.

Returning to Figure 7, the diffraction intensity from the (110) plane appearing at 21.5° becomes lower and the scattering from the amorphous phase at 18.2° becomes stronger with increasing MMA and DAM contents. This tendency becomes more pronounced with increasing temperature. Such a drastic change of the profiles at temperatures of <90°C has never been observed for PE (G201) films.[22] This tendency at elevated temperatures is related to the drastic disappearance of crystallites, showing that the crystallites within EMMA and EDAM films are in a more unstable state than those in branched PE (G201).

Here, it should be noted that for EMMA-III, the intensity distributions appearing at 21.5°, −50, and −110 °C are slightly different from that at 30 °C, although the distributions at −110 and +30 °C were confirmed to be essentially the same for PE (G201) in a preliminary experiment. The slight increase in crystallinity observed at −50 and −110 °C, lower than the β transition[23] (amorphous transition) temperature of PE, is attributed to the local motion of amorphous chain segments of ethylene, which enhance crystallization. Actually, this phenomenon is probably due to the arrangement of amorphous ethylene chains with sufficiently narrow intervals to promote crystallization by small movement of chain fragments owing to the van der Waals force. To pursue a more detailed analysis, the intensity curves were separated into the contribution from the individual crystal planes and the amorphous phase, assuming that each peak had a complex symmetric function given as Gaussian and Lorentzian functions. To give the best fit by computer, the peak separation of each component was carried out on the basis of small changes from the intrinsic diffraction peak position of each crystal plane at room temperatures, as reported elsewhere.[24]

Figure 9 shows the results for EMMA at the indicated temperatures. In these curves, the integrated fractions of the respective crystal components are shown as a dotted line, while a solid line shows the integrated fractions of the first and second components of the amorphous components. A solid line also shows the total composite curve. The integrated fractions of lines obtained by this analysis are given in Table 2 together with their crystal size and peak position, which closely match the observed curve (solid line). Furthermore, crystal size was estimated by Scherrer's equation after the modification by the (331) plane of silicon powder as a reference sample.[25] For EMMA-II, the distribution at 30 °C shows a sharp peak of the (110) reflection and a small duller peak of the (200) reflection in addition to the large broad peak associated with the contribution from the amorphous region. Furthermore, overlapped small peaks for the (020), (011), (310), (111), and (201) planes can be observed at diffraction angles (twice the Bragg angle) higher than 35°. In relation to the DD ^{13}C NMR spectra (Figure 16), the diffraction peak from the (010) plane of the monoclinic crystal form, which is close to the scattering peak from the amorphous phase, was taken into consideration to find the peak separation. At 90 °C, the amorphous contribution becomes larger, while the peak of the (110) reflection becomes smaller, indicating drastic disruption of crystallites. Such behavior has never been observed, even for branched PE (G201).[22] Instead of the disappearance of the reflection from the (020), (011), (310), (111), and (201) planes with low diffraction intensity, the very broad second-order scattering peak from the amorphous phase appears at about 40°.

On the other hand, the profile of EMMA-III at 30 °C shows a small peak from the (110) plane and a very small broad peak from the (200) plane, while the contribution from the amorphous region with the clear second-order scattering occupies most of the total in-

Table 2. Crystallinity Estimated by WAXD Intensity Distribution of EMMA

	EMMA-II		EMMA-III	
temp (°C)	30	90	30	60
crystal content(%) (110) plane	21.6	4.9	8.4	6.0
(200) plane	5.5	1.7	0.6	0.4
other planes	13.6			
content of amorphous phase (%)	59.3	93.4	91.0	93.6
peak position (deg) (110) plane	21.55	21.6	21.6	21.6
(200) plane	23.4	23.4	23.3	23.3
crystal size (nm) (110) plane	7.3	5.2	2.8	2.71
(200) plane	5.38	4.8	1.94	1.63

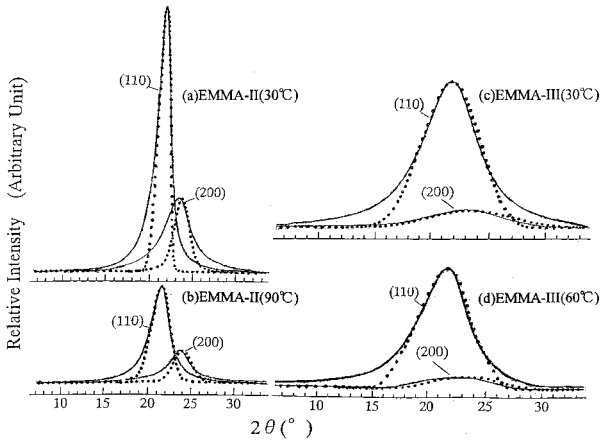

Figure 10. Total WAXD intensity distribution from the (110) and (200) reflections calculated by eq 8 (dotted line) and the experimental results (solid line): (a) EMMA-II at 30 °C; (b) EMMA-II at 90 °C; (c) EMMA-III at 30 °C; (d) EMMA-III at 60 °C.

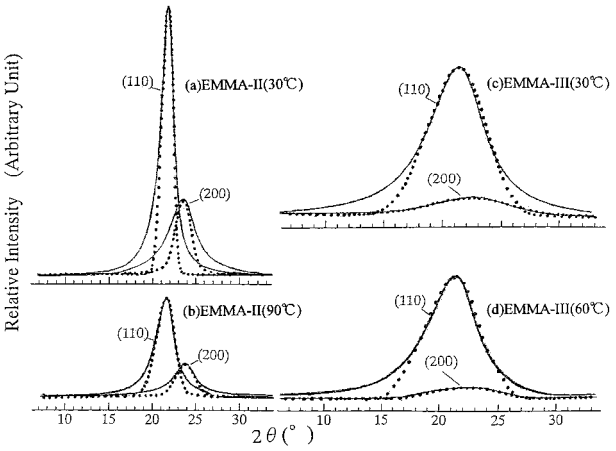

Figure 11. Total WAXD intensity distribution from the (110) and (200) planes reflections calculated by eq 11 (dotted line) and the experimental results (solid line): (a) EMMA-II at 30 °C; (b)EMMA-II at 90 °C; (c) EMMA-III at 30 °C; (d) EMMA-III at 60 °C.

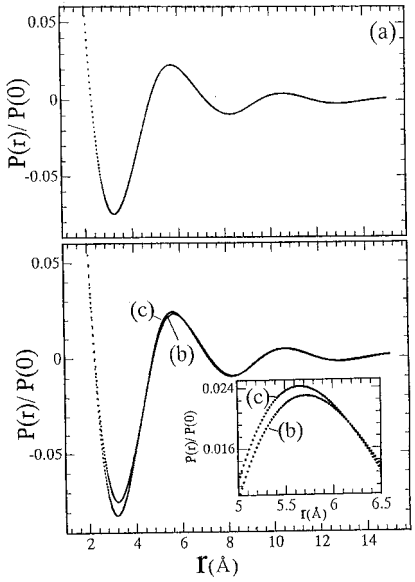

Figure 12. Normalized radial distributions $P(r)/P(0)$ obtained for undrawn EMMA films: (a) EMMA-II at 30 °C; (b) EMMA-III at 30 °C; (c) EMMA-III at 60 °C. $P(r)/P(0)$ must be shown as a solid line but in order to make clear the very small difference between two curves, the results were represented as a dotted line.

tensity distribution. This tendency becomes more pronounced with increasing temperature (Figure 9d). Such second-order scattering from the amorphous phase has never been observed for branched PE (G201), even at 120 °C.[22] Judging from the crystallinity (about 45.6%) of branched PE (G201) films and the very low crystallinity (about 9.0%) of EMMA-II at 30 °C, the appearance of the second peak is thought to be due to the suppression of the crystallization of ethylene sequences, as a result of the repulsion between ethylene and MMA, forcing the amorphous chain segments to induce a highly ordered arrangement. In Table 2, the roughly estimated crystallinity is less than 7% for EMMA-II at 90 °C and less than 9% for EMMA-III at 25 and 60 °C. Of course, such low crystallinity has never been reported for PE (G201), even at elevated temperatures of 100−120°C.[22]

As listed in Table 2, the lengths of the crystallites in the [110] direction and in the direction of the *a* axis are

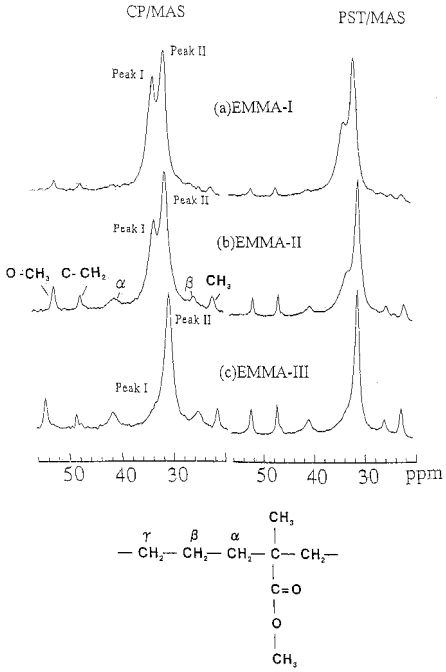

Figure 13. 67.8 MHz CP/MAS and PST/MAS spectra measured for EMMA specimens: (a) EMMA-I; (b) EMMA-II; (c) EMMA-III.

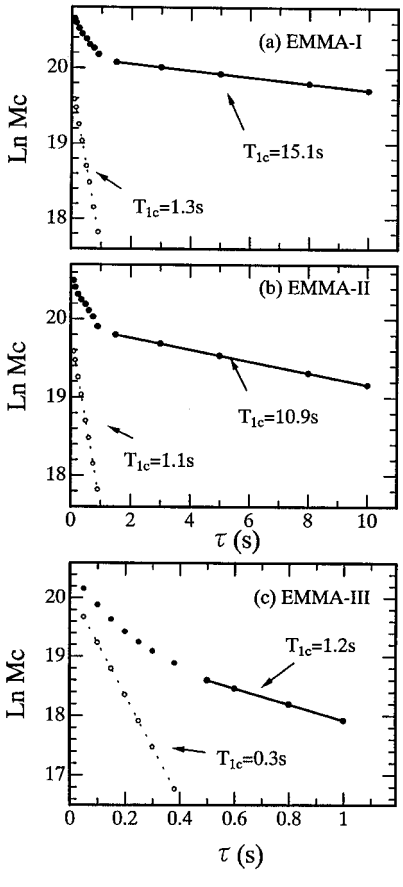

Figure 14. Semilogarithmic plot of the ^{13}C magnetization of the orthorhombic crystal component (peak I) of undrawn EMMA (I, II, and III) films.

less than 3 and 2 nm, respectively, for EMMA-III films. This result implies that the crystallites were constructed by the aggregation of a few ethylene sequences. To confirm this concept, the intensity distributions of the

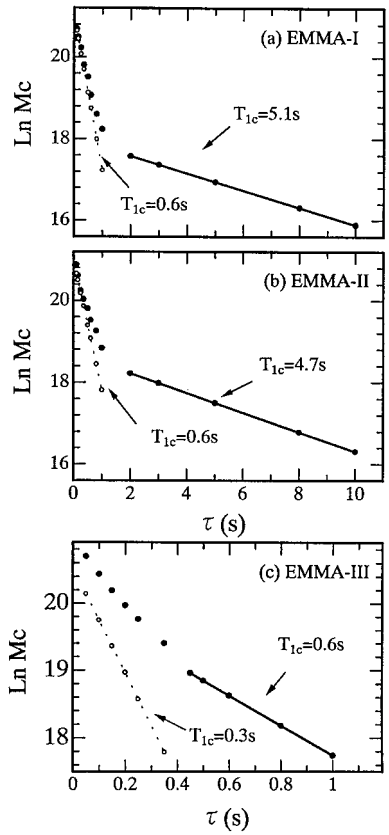

Figure 15. Semilogarithmic plot of the ^{13}C magnetization of the noncrystalline component (peak II) of undrawn EMMA (I, II, and III) films.

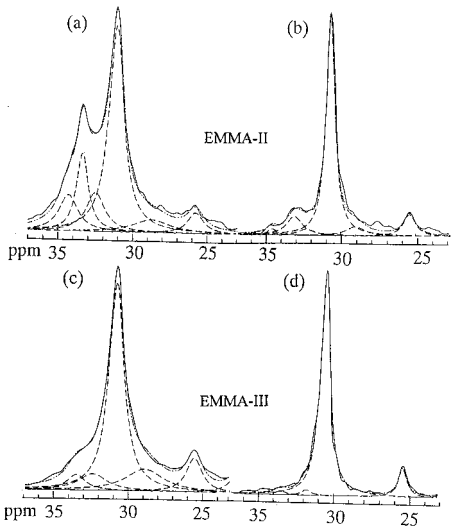

Figure 16. Component analysis of the total DD ^{13}C NMR spectra for undrawn EMMA specimens at the indicated temperatures: (a) EMMA-II at 27−36 °C; (b) EMMA-II at 60−64 °C; (c) EMMA-III at 27−36 °C; (d) EMMA-III at 60−64 °C.

(110) and (200) planes were calculated from the product of the Laue function and the structural factor by assuming that a crystal unit of EMMA corresponds to a PE crystal unit. Assuming the number of crystal units in the directions of the *a*, *b*, and *c* axes to be N_1, N_2, and N_3, respectively, the diffraction intensity as a function of the Bragg angle θ may be given by

$$I = E^2 \tag{1}$$

where

$$E = L \times F_{hkl} \tag{2}$$

In eq 2, L and F_{hkl} are the Laue function and the structural factor, respectively. They are given by

$$L = [\sin(2\pi N_1\, hd \sin\theta/\lambda')\sin(2\pi N_2\, kd \sin\theta/\lambda')\sin(2\pi N_3\, ld \sin\theta/\lambda')]/[\sin(2\pi hd \sin\theta/\lambda')\sin(2\pi kd \sin\theta/\lambda')\sin(2\pi ld \sin\theta/\lambda')] \tag{3}$$

and

$$F_{hkl} = 2f_c \cos[2\pi m_c(h \cos\theta_V \cos\omega/a + k \cos\theta_V \sin\omega/b)] + 2f_c \exp\{\pi(h+k)\}\cos[2\pi m_c(-h \cos\theta_V \cos\omega/a + k \cos\theta_V \sin\omega/b)] \tag{4}$$

where f_c is atomic scattering factor of carbon given as a function of θ. θ_V is half of the valence angle of the C−C bonds, and ω is the angle between the *a* axis and the shadow axis of the main chains on the *ab* plane of a crystal unit. On the basis of the geometrical arrangement of a PE crystal unit, the values of θ_V and ω are given as 54.8 and 39°, respectively.[24]

Judging from the broad diffraction peak profile due to small and unstable crystallites, it is evident that the position of the specimen sampled by the X-ray beam contains distributions of the number of crystal units N_1, N_2, and N_3. The size distributions are also determined by assuming that the numbers of crystal units in the directions of the *a*, the *b*, and *c* axes have the distribution functions $P(N_1)$, $P(N_2)$, and $P(N_3)$, respectively, as follows:

$$P(N_1) = \exp\left[-\frac{(N_1-\bar{N}_1)^2}{2\sigma_{N_1}^2}\right] \Big/ \sum_{N_1=1}^{2\bar{N}_1-1} \exp\left[-\frac{(N_1-\bar{N}_1)^2}{2\sigma_{N_1}^2}\right] \tag{5}$$

$$P(N_2) = \exp\left[-\frac{(N_2-\bar{N}_2)^2}{2\sigma_{N_2}^2}\right] \Big/ \sum_{N_2=1}^{2\bar{N}_2-1} \exp\left[-\frac{(N_2-\bar{N}_2)^2}{2\sigma_{N_2}^2}\right] \tag{6}$$

$$P(N_3) = \exp\left[-\frac{(N_3-\bar{N}_3)^2}{2\sigma_{N_3}^2}\right] \Big/ \sum_{N_3=1}^{2\bar{N}_3-1} \exp\left[-\frac{(N_3-\bar{N}_3)^2}{2\sigma_{N_3}^2}\right] \tag{7}$$

where $\bar{N}_1$, $\bar{N}_2$, and $\bar{N}_3$ are the average numbers of the crystal units in the directions of the *a*, *b*, and *c* axes, respectively, and σ_{N_1}, σ_{N_2}, and σ_{N_3} are the corresponding standard deviations. Consequently, the diffraction intensity $\langle I\rangle$ in a real system may be given by

$$\langle I\rangle = \sum_{N_1=1}^{2\bar{N}_1-1}\sum_{N_2=1}^{2\bar{N}_2-1}\sum_{N_3=1}^{2\bar{N}_3-1} P(N_1)P(N_2)P(N_3)I \tag{8}$$

Figure 10 shows the calculated distributions (dotted curve) and experimental diffractions (solid curve) of intensity distributions for the (110) and (200) planes for EMMA-II at 30 and 90 °C and those for EMMA-III at 30 and 60 °C. The solid curves are enlargements of the curves obtained after peak separation (Figure 9). Since

Table 3. Length Fluctuation of the *a* Axis Used for Numerical Calculation of Eq 11

	$\bar{N}_1 = 3$	$\bar{N}_1 = 5$	$\bar{N}_1 = 7$
a_1	0.740	0.740	0.740
a_2	0.750	0.745	0.745
a_3	0.760	0.750	0.750
a_4	0.770	0.755	0.7525
a_5	0.780	0.760	0.755
a_6		0.765	0.758
a_7		0.770	0.760
a_8		0.775	0.765
a_9		0.780	0.675
a_{10}			0.770
a_{11}			0.7725
a_{12}			0.775
a_{13}			0.780

an absolute comparison between the experimental and calculated distributions is impossible, the calculated distribution is normalized by the experimental peak height of the (110) plane. The relative intensity ratio between the (110) planes and (200) planes for the theoretical calculation was determined by considering that from the experimental results. To pursue the numerical calculation, the value of $\bar{N}_1$ can be postulated from the crystal size in the direction of the *a* axis. Furthermore, $\bar{N}_2 = 2\bar{N}_1$ is adopted on the basis of the concept that the crystal size in the [110] direction is bigger than that in the *a* axis experimentally, and the crystal lamella axis of PE corresponds to the *b* axis. $\bar{N}_3$ is independent of the normalized diffraction profile for the (*hk*0) planes but depends on the intensity, thus ensuring $\bar{N}_3 = \bar{N}_1$. The parameters σ_{N_1}, σ_{N_2}, and σ_{N_3} are fixed at 5, 3, and 3, respectively.

As shown in Figure 10, the peak becomes broader with a decreasing number of $\bar{N}_1$. The calculated results are in fairly good agreement with the experimental results except for the peak positions of the (110) and (200) reflections. It can be seen that the small crystallites with $\bar{N}_1 = 3$ and $\bar{N}_2 = 6$ provide a clear peak profile of the (110) plane. Accordingly, small crystallites with size distribution can be detected by X-ray diffraction and the peak separation for EMMA-III shown in Figure 9 can be justified.

Returning to Table 2, the peak position of the (200) reflection appears at 23.4°, which shifts to a lower diffraction angle from 24.0° as has been reported for a PE crystal unit.[25] The longer distance between the (200) planes for the EMMA specimens is thought to be due to the fluctuation of the crystal lattice in the direction of the *a* axis. The origin of this fluctuation is due to residual stress[26] and/or unstable lattice formation. Moreover, the peak position of the (110) reflection appearing at 21.5° is also due to the small shift from 21.6°. This is obviously attributed to the fluctuation of the *a* axis.

To satisfy the experimental results in Figure 9, the fluctuation effect of the distance between the (200) planes is introduced in the case of $\bar{N}_1 = 3-7$. The distance of a_n ($n = 3-7$) is determined by postulating that the length of the *a* axis within EMMA is longer than the normal length, 0.74 nm, observed for PE generally and the values are listed in Table 3. As the most probable possibility, the value of the length of the *a* axis is determined to be 0.76 nm from the experimental peak top of the (200) reflection. The reference length of 0.76 nm is set as a_3 at $\bar{N}_1 = 3$, a_5 at $\bar{N}_1 = 5$, and a_7 at $\bar{N}_1 = 3$. The value of a_1 is set to be 0.74 nm, corresponding to the peak position at 24.0°,and the other values of a_n are given arbitrarily to ensure the symmetrical distribution of $P(a_n)$. The fluctuation in the *b* axis is neglected to avoid an increase in parameters. Thus, we have

$$P(a_n) = \exp\left[-\frac{(a_n - \bar{a})^2}{2\sigma_a^2}\right] \Big/ \sum_{n=1}^{2\bar{N}_1-1} \exp\left[-\frac{(a_n - \bar{a})^2}{2\sigma_a^2}\right] \quad (9)$$

and

$$P(d_n) = \exp\left[-\frac{(d_n - \bar{d})^2}{2\sigma_d^2}\right] \Big/ \sum_{n=1}^{2\bar{N}_1-1} \exp\left[-\frac{(d_n - \bar{d})^2}{2\sigma_d^2}\right] \quad (10)$$

where d_n is given by $a_n b/\sqrt{a_n^2+b^2}$. Of course, a_n in Table 3 is used instead of *a* in eq 4. By using eq 10, eq 8 can be rewritten as

$$\langle I \rangle = \sum_{N_1=1}^{2\bar{N}_1-1} \sum_{N_2=1}^{2\bar{N}_2-1} \sum_{N_3=1}^{2\bar{N}_3-1} \sum_{n=1}^{2\bar{N}_1-1} P(d_n)P(N_1)P(N_2)P(N_3)I \quad (11)$$

Figure 11 shows the results calculated with eq 11. The parameters σ_a and σ_d are fixed at unity. With increasing lattice fluctuation in the direction of the *a* axis, the relative intensity of the (200) plane becomes slightly broader than that shown in Figure 9, although the difference is too small to recognize. The reflection peak of the (200) plane shifts toward the lower side to 23.4°, and the reflection of the (110) plane shows a peak at 21.5°. The calculated curve is in good agreement with the experimental one. This is one of the quantitative assumptions postulated from a series of experimental results showing that the crystallites within EMMA films are in an unstable state in comparison with branched PE (G201). The temperature factor was neglected in the above numerical calculations.

Returning to Figure 9, the scattering from the amorphous phase depends on MMA content and measured temperature. To check this, the structure of the amorphous phase is estimated by the radial distribution $P(r)$. The scattered intensity $I(b)$ may be given by the radial distribution generally as follows:

$$I(b) = \int_0^\infty 4\pi^2 P(r) \frac{\sin br}{br}\, dr \quad (12)$$

Here

$$b = \frac{4\pi}{\lambda} \sin\theta \quad (13)$$

By the Fourier transformation of $I(b)$, $P(r)$ may be given by

$$P(r) = \frac{1}{2\pi^2} \int_0^\infty I(b) br \sin br\, db \quad (14)$$

At $r = 0$, we have

$$P(0) = \frac{1}{2\pi^2} \int_0^\infty b^2 I(b)\, db \quad (15)$$

Equation 15 denotes an invariant that is independent of the structure of the scattering system. To simplify the analysis, eq 14 may be normalized by eq 15, in which

the first-order scattering was used as $I(b)$ in the numerical calculation.

Figure 12 shows $P(r)/P(0)$: curve a obtained for EMMA-II at 30 °C and curves b and c for EMMA-III at 30 and 60 °C respectively. The maximum peak position of $P(r)/P(0)$ appearing at $r = 5.7$ Å (0.57 nm) is independent of temperature, but the magnitude for the EMMA-II film at 30 °C becomes slightly lower than that of the others. For EMMA-III films, the very small difference at 30 and 60 °C can be recognized by the enlargement in Figure 12b. Namely, the magnitude depends on the profile of the amorphous scattering. In comparison with the experimental diffraction intensity distribution in Figure 9, the amorphous scattering with the second-order maximum provides a slightly higher magnitude of $P(r)/P(0)$, reflecting an ordered arrangement of the amorphous chains, while the corresponding diffraction peaks from the crystal planes become broader. This result quantitatively justifies to the proposed concept that the suppression of the crystallization by MMA side groups induces ordering of the amorphous chain segments.

Apart from the above static information, the morphology of crystalline and amorphous phases within EMMA films was investigated by high-resolution solid state ^{13}C NMR. Such an investigation of EMMA has never been reported, but the spectra of analyzed EMMA could be compared with the spectra of EDAM[9] and PE (G201).[22]

3.3. Dynamic Properties by ^{13}C NMR. Figure 13 shows the 67.8 MHz CP/MAS and PST/MAS ^{13}C NMR spectra of EMMA-I, EMMA-II, and EMMA-III films ($\lambda = 1$) ranging from 20 to 56 ppm at room temperature. These spectra are shown first to explain the outline of our NMR experiments. As is known for semicrystalline polymers, CP/MAS spectra emphasize the contribution of the crystalline phase, while PST/MAS spectra acquired with a short repetition time emphasize the contribution of the amorphous phase. The CP/MAS spectrum of EMMA-I shows two peaks with chemical shifts of 32.81 ppm (peaks I) and 30.76 ppm (peaks II), which can be assigned to the orthorhombic crystalline and noncrystalline methylene carbons in the ethylene sequence, respectively.[27−30] The magnitude of peak II is higher than that of the peak I in the CP/MAS spectrum, indicating that even the crystallinity of EMMA-I with the lowest MMA content is much lower than that of PE. Of course, the relative intensity of peak I becomes smaller with increasing MMA content, as shown for EMMA-II and EMMA-III films. This tendency becomes more pronounced for the PST/MAS spectrum, and the contribution from the orthorhombic crystal shows as a shoulder at 32.81 ppm.

The assignment of the other peaks was made according to the DD/MAS spectra of EDAM reported elsewhere[9] as well as the solution NMR spectra.[8] In a series of the spectra, the signals of α and β carbons and signals corresponding to the DAM unit are greatly enhanced in reverse proportion to the orthorhombic signal in the PST/MAS spectra. The signal of the γ carbon shall be discussed later. This indicates that the two CH_2 units neighboring the MMA along the ethylene sequences are located outside the crystalline regions. The mobility of the MMA side groups as a function of temperature will be discussed elsewhere in relation to positron annihilation.[31]

On the basis of the above results, ^{13}C spin−lattice relaxation time (T_{1C}) was measured by Torchia or by the standard saturation−recovery pulse sequence to inquire whether each resonance line comprises a single component.

Table 4. ^{13}C NMR Spin−Lattice Relaxation Time (T_{1C}) for Undrawn EMMA Films by Torchia and Standard Saturation Recovery Pulse Sequence[a]

	T_{1C} (s) (by Torchia)					T_{1C} (s) (by saturation recovery)	
	crystalline component			noncrystalline component			
specimen	C_o			I	R	C_o	noncrystalline component
EMMA-I		15.1	1.3	5.1	0.6		
EMMA-II		10.9	1.1	4.7	0.6		
EMMA-III		1.2	0.3	0.6	0.3	1.5	0.3
LDPE (G201)[b]	145	15.8	1.27	0.375			

[a] Key: C_o, orthorhombic crystal form; I, interfacial component; R, rubbery component. [b] The data of LDPE were from ref 22.

Figure 14 shows the variation of the relative intensity of peak I measured by Torchia's pulse sequence[32] as a function of decay time τ for the three EMMA specimens. Peak deconvolution was carried out on each partially relaxed spectrum due to the overlapping of peak I and peak II. It is obvious that all of the T_{1C} decay curves in Figure 14 exhibit biexponential decay behavior. The two corresponding T_{1C} values of the orthorhombic crystal for each specimen were obtained by least-squares fitting of the decay curves and are listed in Table 4.

As for EMMA-III, the decay in the plots of ^{13}C magnetization againstt for the orthorhombic crystalline and noncrystalline components was too rapid decay to obtain a decay curve by Torchia. To confirm the accuracy of the T_{1C} value, the standard saturation−recovery pulse sequence was adopted. The logarithm of ^{13}C magnetization ensures a linear relationship at $\tau < 2.5$ s. The highest peak top for the orthorhombic crystalline component could be detected clearly by varying values of t. These results are summarized in Table 4. T_{1C} values of peak I by the standard saturation−recovery pulse sequence was 1.5 s. This value is in good agreement with the longer value (1.2 s) of the orthorhombic crystal form measured by Torchia's sequence.

Figure 15 shows the plots of the peak II around 30.76 ppm obtained after the peak separation discussed above. The intensity of ^{13}C magnetization against τ can also be classified into two components by using a least-squares method with a computer: a slow decay line and a rapid decay line. The initial slope of each decay curve yields T_{1C}. Two kinds of T_{1C} values estimated from the initial slope of each decay curve are listed in Table 4. Such an interesting behavior has never been observed for PE.[22] For EMMA-III, the T_{1C} value measured by the standard saturation−recovery pulse sequence was 0.3 s. This value is equal to the shorter value (0.3 s) of the amorphous (noncrystalline) region measured by Torchia's sequence. In Table 4, it is evident that the shorter T_{1C} values of peak I corresponding to the crystalline phase were shorter than the longer T_{1C} values of peak II associated with the amorphous component. This is quite different from the decay behavior of PE. In previous works,[22] it has been reported that the orthorhombic crystal of the PE form has three different values of T_{1C}. The values of G201 melt film (branched PE) are listed in Table 4 as a reference. The shortest value of the orthorhombic crystal component of PE is longer than

the value of the noncrystalline component, and the same tendency was confirmed for other PE samples. Here it may be noted that the orthorhombic crystal within EMMA films has no decay time beyond 100 s, as has been confirmed for PE (G201) film. Namely, the longest T_{1C} of the orthorhombic crystal of EMMA is much shorter than that of the PE (G201) film. This supports the X-ray diffraction data of EMMA crystallites with very small crystallinity, very small crystal size, and the lattice expansion listed in Table 2. The longer and shorter T_{1C} values of the noncrystalline component are thought to be due to interfacial and rubbery states, respectively. The longer T_{1C} beyond 0.6 s has never been observed for PE.[22] The shorter T_{1C} value for each specimen is close to the T_{1C} value observed for PE. This indicates that an interfacial component associated with a longer T_{1C} is attributed to a highly ordered molecular arrangement of ethylene sequences. Namely, the amorphous phase (noncrystalline phase) within EMMA film consists of ordered structures whose orientation fluctuation is smaller than that of PE, since the MMA side groups suppress the crystallization associated with an essential property of ethylene sequences. The difficulty in accelerating the self-arrangement of ethylene sequences as crystallites, which is due to strong repulsion of MMA and ethylene, allows an ordered arrangement of amorphous ethylene sequences rather than a random orientation. X-ray intensity distributions in Figure 9 support the results in Table 4. As shown in Figure 9, the amorphous halo shows the second peak associated with the ordered arrangement of amorphous chain segments. This phenomenon has never been observed for branched PE (G201) films.[22]

Here, we shall refer briefly to the problem of estimating T_{1C} in the present paper. Schmidt-Rohr and Spiess have reported that solid-state chain diffusion between the crystalline and amorphous (noncrystalline) phases in linear PE at temperatures down to −173 °C can be detected by two-dimensional and one-dimensional exchange ^{13}C NMR experiments under the MAS condition.[33] They explained chain diffusion in terms of NOE factor and nonexponential T_{1C} in the crystallites, as well as the dependence of T_{1C} on the crystallite thickness reported by Axelson et al.,[34] by excluding the possibility of ^{13}C spin diffusion to the exchange of magnetization between the amorphous and crystalline phases. Recently, Hu et al. studied the occurrence and rate of 180° chain flip motions in the crystalline region of high-density PE and ultrahigh molecular weight PE by dipolar ^{13}C NMR. They pointed out that the jumps occur between two sites, with a rotation angle of 180°and a jump rate of $\sim$10 s^{-1} at ambient temperature, and the activation energy for the 180° chain flip was 93 ± 10 kJ/mol.[35] In the present system, chain diffusion is thought to be more extensive than the above two PE samples. If the chain diffusion occurs mainly at the exterior of the orthorhombic crystals, the orthorhombic crystals then exhibit different morphologies at the exterior and interior. This leads to the multiexponential ^{13}C spin−lattice relaxation decay behavior of the orthorhombic crystals of the samples studied in this paper.

Figure 16 shows the DD/MAS ^{13}C NMR spectra without CP obtained for EMMA-II and EMMA-III at elevated temperatures. Since the waiting time was set at longer than 5 times the longest T_{1C} for each sample, these spectra reproduce the contributions from all of the structural components quantitatively. The methylene peaks of all spectra were deconvolved by computer fitting into four components, namely orthorhombic, monoclinic, interfacial, and rubbery. The initial values of all components were given by adopting the corresponding chemical shifts of G201 obtained elsewhere[22] (listed in Table 5 as a reference). In addition to the four components, a peak appeared at about 29 ppm, except for the spectrum measured for EMMA-III at 60−64 °C. This peak is thought to be the contribution from γ-CH_2 (Figure 13) associated with an more entities with ordered degree. Although the line corresponding to the orthorhombic crystal form with a peak at about 33 ppm consists of two components with different T_{1C}, both components were assumed to have the same line shape. The purpose of the spectrum analysis is to estimate crystallinity by ^{13}C NMR. Actually, it has been reported that the integrated fraction of the crystal line is in good accord with the degree of crystallinity estimated by ^{1}H broad-line NMR analysis, and the latter coincides with values obtained from density measurements.[36,37] The integrated fractions of the respective components are shown as a dashed line. The composite curve is shown by a dotted line, which closely reproduces the observed spectrum (solid line). The integrated intensity fraction and the corresponding chemical shifts thus obtained are listed in Table 5.

Table 5. ^{13}C NMR Chemical Shifts and Mass Fractions of the Respective Components at the Indicated Temperature Measured for EMMA Films[a]

specimen	temp (°C)	chemical shifts (ppm)				mass fraction (%)			
		C_o	C_m	I	R	C_o	C_m	I	R
EMMA-II	27−36	33.4	34.3	32.5	30.9	16.9	12.4	13.4	37.3
	60−64	33.1	34.6	32.3	30.7	12.9	2.3	3.8	81.0
EMMA-III	27−36	33.5		32.4	30.9	7.6		12.3	80.1
	60−64	33.5		31.8	30.7	2.0		2.5	95.5
LDPE (G201)[b]	27−36	33.0	34.8	31.5	30.9	42.1	7.2	23.7	27.9
	60−64	33.1	34.9	31.5	30.9	38.8	6.6	19.4	35.2

[a] Key: C_o, orthorhombic crystal form; C_m,monoclinic crystal form; I, interfacial component; R, rubbery component. [b] The data of LDPE were from ref 22.

It was observed that the chemical shift of each component is nearly independent of the MMA content and temperature. The mass fraction of the monoclinic crystal form[24] within EMMA-II and EMMA-III films disappeared at elevated temperature. Interestingly, the mass fraction of the monoclinic form within EMMA-II film at room temperature is more than 12%, although the monoclinic crystal form was not observed by X-ray diffraction (Figure 9). The interfacial region for EMMA-II and EMMA-III films decreased at elevated temperature, and this tendency cannot be obtained by X-ray diffraction. This indicates that ^{13}C NMR has an advantage in determining the phase structure of crystalline polymers. It should be noted that an exact estimation for the mass fraction in the interfacial region by X-ray scattering is generally difficult except when crystal lamellae are highly oriented with large flat faces and the difference of density between the crystal and amorphous regions is very large.[38] For the present EMMA films, the estimation of the interfacial thickness was impossible on the basis of X-ray diffraction. As another problem, the crystallinity by density measurement must be estimated on the basis of the simple assumption that the specimen consists of two phases, the crystalline and amorphous (noncrystalline) phases. Thus, the density measurements are also unable to provide any information about the interfacial region.

Table 6. Crystallinity Estimated by DD ^{13}C NMR Spectra and X-ray Diffraction Profile for EMMA Films

		crystallinity	
specimen	temp (°C)	^{13}C NMR	X-ray
EMMA-II	30		31.7
	27−36	39.3	
	60−64	15.2	
	90		5.6
EMMA-III	30		9.0
	27−36	7.6	
	60−64	2.0	
	60		6.4
LDPE (G201)[a]	30		55.3
	27−36	48.4	
	60−64	45.4	
	70		50.7

[a] The data of LDPE were from ref 22.

Total mass fraction of the orthorhombic and monoclinic crystals can be estimated as crystallinity of the given specimens at the indicated temperatures. The results are listed in Table 6 together with the results estimated by X-ray diffraction. At room temperature, the crystallinity by ^{13}C NMR is in good agreement with that by X-ray diffraction. Interestingly, the crystallinity, corresponding to total mass fractions of the orthorhombic crystal and the monoclinic crystal estimated by ^{13}C NMR, is almost equal to the crystallinity estimated as a fraction of the orthorhombic crystal by X-ray diffraction.

At elevated temperatures, the results by ^{13}C NMR tend to deviate from those of X-ray diffraction. The difference is probably due to the different experimental conditions: the ^{13}C NMR data were obtained with the length allowed to change freely during measurement at elevated temperatures, while the X-ray data were obtained with fixed length by clamping the film between two metallic clamps. In our NMR instrument, it is impossible to set the specimen to a fixed length in the cylinder-type sample tube. In any case, it is evident that the crystallinity of the EMMA films drastically decreased with temperature, although the degree of decrease for branched PE (G201) is not so remarkable.[22] This is due to the fact that small EMMA crystallites are unstable and a number of defects as well as residual inner stress.

Because of the strong repulsion of MMA and ethylene, the MMA side groups suppress the crystallization associated with an essential property of ethylene sequences and local aggregation of a few ethylene sequences provides small and unstable crystallites. The difficulty in accelerating the self-arrangement of ethylene sequences to form crystallites allows an ordered arrangement of ethylene sequences in the amorphous phase rather than a random orientation. Accordingly, we may expect that since the amorphous chain segments do not behave like random work chains, the possibility of making entanglements becomes lower as MMA content increases. Furthermore, this phenomenon ensures greater drawability (10 times) of EMMA (EMMA-III) films than PE. This analysis is based on the concept that the large difference of drawability between PE dry gel films and melt films is attributed to the number of entanglements. According to previous studies,[39] the drawability of PE dry gel films depends principally on the concentration of solution from which a gel is made. This phenomenon is attributed to the reduced number of entanglements per molecule in solution cast/spun polymers compared to those obtained from the melt. Recently, Psarski et al. proposed very important phenomena for the possibility of obtaining a linear PE melt in which the polymer chains are disentangled.[40] The possibility was discussed on the basis of the reputation theory and the verified experiments. In their samples, a custom-made pressure cell was used to ensure high-pressure crystallization. As a result, large chain-extended crystals contained no entanglements and the crystallinity was about 93%. They pointed out that because the chain-extended crystal basal surfaces contained very few chain folds, the chains were only subjected to entropy-driven coiling, which does not markedly increase the number of tight entanglements. Their concept can be applied to the present system. If the amorphous chains with an ordered arrangement more or less form crystallites, it is evident that the possibility of forming entanglements becomes very low. The existence of extended segments was also reported by Merrets.[13] Actually, no spherulite associated with folded chains could be observed for undrawn EMMA films under Hv polarization.

Through a series of experimental results, it was found that small unstable crystallites lead to the mechanical behavior shown in Figures 1, 2, and 4. The few entanglements and the presence of very few crystallites as cross-linking points ensure the same recycle routes of stress−strain curves of the EMMA films ($\lambda < 2$) up to 40 times at room temperature. Despite such behavior being similar to rubber elasticity, the drastic stress relaxation confirmed at elevated temperatures is attributed to the disappearance of unstable crystallites that function as cross-linking points. The disappearance induces drastic chain slippage, and thus drastic stress relaxation occurs.

4. Conclusions

The relationship between the morphology and the mechanical properties of EMMA films with different MMA contents (EMMA-I with 3.0 mol %, EMMA-II with 6.5 mol %, and EMMA-III with 14.6 mol %) were investigated as a function of temperature by using polarized light scattering, X-ray diffraction, and ^{13}C solid-state NMR. X-ray diffraction measurement revealed that the crystallites within EMMA films are much smaller than those within branched PE (G201) film and that the crystallinity is much lower. Furthermore, the number of crystallites drastically decreased as temperature increased. This indicates the presence of unstable crystallites with a disordered lattice. On the other hand, the intensity distribution from the amorphous phase showed the first and second scattering maxima, indicating that the ethylene sequences in the amorphous phase has an ordered arrangement rather than a random orientation. ^{13}C NMR measurements revealed that the overall decay curves for the orthorhombic crystals and the amorphous phase could be classified into two components, i.e., a slow decay curve and a rapid decay curve, indicating the existence of two kinds of T_{1C}. The shorter T_{1C} value for the orthorhombic crystal was shorter than the longer T_{1C} values of the amorphous component, indicating crystallites with unstable lattice formation. These results were in good agreement with those estimated by X-ray. The EMMA (EMMA-III) film with a maximum draw ratio of 10 times at room temperature provided a reversible change of stress−strain curves when the specimen was stretched

up to 2 times at room temperature. Even so, stress relaxation occurred as the temperature of the EMMA film (EMMA-III) increased. This is out of the framework of rubber elasticity. The high draw ratio is obviously due to the smaller number of entanglements per molecule in comparison with PE. Because of the strong repulsion of MMA and ethylene, the MMA side groups suppress the crystallization associated with an essential property of ethylene sequences. Furthermore, the difficulty in accelerating self-arrangement of the ethylene sequences as crystallites leads to a local ordered arrangement of the ethylene sequences rather than a random orientation in the amorphous phase. The drastic decrease in stress at a constant strain with temperature can be considered molecular slippage due to the disappearance of unstable crystallites that function as crosslinking points and induce rubber elasticity.

Acknowledgment. We are indebted to Dr. Fujita, Sumitomo Chemical Co. Ltd., for his valuable comments.

References and Notes

(1) Flory, P. J. *Principles of Polymer Chemistry*; Cornell University Press: New York, 1953; p 602.
(2) Yeh, G. S. Y. *J. Macromol. Sci., Phys.* **1972**, *B6*, 451.
(3) Pechold, W.; Hauber, M. E. T.; Liska, E.; Kolloid-Z. *Z. Polym.* **1973**, *251*, 818.
(4) Vollmert, B.; Stutz, H. *Makromol Chem.* **1968**, *3*, 182.
(5) Cotton, J. P.; Decker, D.; Benoit, H.; Farnoux, B.; Higgins, J.; Jannink, G.; Ober, R.; Picot, C.; des Cloizeaux, J. *Macromolecules* **1974**, *7*, 863.
(6) Hayashi, H,; Hamada, F.; Nakashima, A. *Macromolecules* **1976**, *9*, 543.
(7) Ohmae. T.; Hosoda, S.; Tanaka, H.; Kihara, H.; Jiang, B.; Ying, Q.; Qian, R.; Masuda, T.; Nakajima, A. *Pure Appl. Chem.* **1993**, *65*, 1825.
(8) Chen, Q.; Luo, H. J.; Yang, G.; Xu, D. F. *Polymer* **1997**, *38*, 1203.
(9) Luo, H.-J.; Chen, Q.; Yang, G.; Xu, D. *Polymer* **1998**, *39*, 943.
(10) Rische, T.; Waddon, A. J.; Dickinson, L. C.; MacKnight, W. J. *Macromolecules* **1998**, *31*, 1871.
(11) VanderHart, D. L.; Perez, E. *Macromolecules* **1986**, *19*, 1902.
(12) Perez, E.; VanderHart, D. L. *J. Polym. Sci. Polym. Phys. Ed.* **1987**, *25*. 1637.
(13) Merrett, F. M. *J. Polym. Sci.* **1957**, *24*, 467.
(14) Rhodes, M. B.; Stein, R. S. *J. Polym. Sci., Part A-2* **1969**, *7*, 1538.
(15) Stein, R. S.; Rhodes, M. B. *J. Appl. Phys.* **1960**, *31*, 1873.
(16) Motegi, M.; Oda, T.; Moritani, M.; Kaw ai, H. *Polym. J.* **1970**, *1*, 209.
(17) Hashimoto, T.; Stein, R. S. *J. Polym. Sci., Part A-2* **1971**, *9*, 1747.
(18) Sawatari, C.; Muranaka, T.; Matsuo, M. *Polym. J.* **1983**, *15*, 33.
(19) Sawatari, C.; Iida, M.; Matsuo, M. *Macromolecules* **1984**, *17*, 1765.
(20) Iida, M.; Sawatari, C.; Matsuo, M. *J. Chem. Soc., Faraday Trans 2* **1984**, *80*, 1599.
(21) Piorkowska, E.; Galeski, A.; Kryszewski, M. *Colloid Polym. Sci.* **1982**, 260, 735.
(22) Shimizu, Y.; Harashina, Y.; Sugiura, Y.; Matsuo, M. *Macromolecules* **1995**, *28*, 6889.
(23) Kawai, H.; Suehiro, S.; Kyu, T.; Shimomura, A. *Polym. Eng. Rev.* **1983**, *3*, 109.
(24) Sawatari, C.; Matsuo, M. *Colloid Polym. Sci.* **1985**, *263*, 783.
(25) Swan, P. R. *J. Polym. Sci.* **1962**, *56*, 409.
(26) Bates, F. S.; Cohen, R. E.; Argon, A. S. *Macromolecules* **1983**, *16*, 1108.
(27) Earl, W. L.; VanderHart, D. L. *Macromolecules* **1979**, *12*, 762.
(28) VanderHart, D. L.; Khoury, F. *Polymer* **1984**, *25*, 1589.
(29) Ando, I.; Yamanobe, T.; Sorita, T.; Komoto, T.; Sato, H.; Deguchi, K.; Imanari, M. *Macromolecules* **1984**, *17*, 1955.
(30) Ando, I.; Sorita, T.; Yamanobe, T.; Komoto, T.; Sato, H.; Deguchi, K.; Imanari, M. *Poymer* **1985**, *26*, 1864.
(31) In preparation as a continuation of this paper.
(32) Torchia, D. A. *J. Magn. Reson.* **1978**, *36*, 91.
(33) Schmidt-Rohr, K.; Spiess, H. W. *Macromolecules* **1991**, *24*, 5288.
(34) Axelson, D. E.; Mandelkern, L.; Popli, R.; Mathieu, P. *J. Polym. Sci., Polym. Phys. Ed.* **1983**, *21*, 2319.
(35) Hu, W.-G.; Boeffel, C.; Schmidt-Rohr, K. *Macromolecules* **1999**, *32*, 1611.
(36) Kitamaru, R.; Horii, F.; Hyon, R. St. J. *J. Polym. Sci., Polym. Phys. Ed.* **1977**, *15*, 821.
(37) Kitamaru, R.; Horii, F. *Adv. Polym. Sci.* **1978**, *26*, 137.
(38) Sawatari, C.; Okumura, T.; Matsuo, M. *Polym. J.* **1986**, *18*, 741.
(39) Ogita, T.; Yamamoto, R.; Suzuki, N.; Ozaki, F.; Matsuo, M. *Polymer* **1991**, *32*, 822.
(40) Psarski, M.; Piorkowski, E.; Galeski, A. *Macromolecules* **2000**, *33*, 916.

MA002110W